ALMA ACA detection of submillimeter emission associated with the west hot spot of the radio galaxy Pictor A

Naoki Isobe, 1 Hiroshi Nagai, 2,3 Motoki Kino, 4,2 Shunsuke Baba, 5,2 Takao Nakagawa, 1 Yuji Sunada, 6 and Makoto Tashiro 1,6

- ¹ Institute of Space and Astronautical Science (ISAS), Japan Aerospace Exploration Agency (JAXA), 3-1-1 Yoshinodai, Chuo-ku, Sagamihara, Kanagawa, 252-5210, Japan
 - $^2\ National\ Astronomical\ Observatory\ of\ Japan,\ 2\text{-}21\text{-}1\ Osawa,\ Mitaka,\ Tokyo,\ 181\text{-}8588,\ Japan}$
- ³ Department of Astronomical Science, The Graduate University for Advanced Studies, SOKENDAI, 2-21-1 Osawa, Mitaka, Tokyo 181-8588, Japan
- ⁴ Kogakuin University of Technology & Engineering, Academic Support Center, 2665-1 Nakano, Hachioji, Tokyo, 192-0015, Japan
- ⁵ Graduate School of Science and Engineering, Kagoshima University, 1-21-35 Korimoto, Kagoshima, Kagoshima 890-0065, Japan
 ⁶ Department of Physics, Saitama University, 255 Shimo-Okubo, Sakura-ku, Saitama, 338-8570, Japan

ABSTRACT

In order to investigate the far-infrared excess detected from the west hot spot of the radio galaxy Pictor A with the Herschel observatory, a submillimeter photometry is performed with the Atacama Compact Array (ACA) of the Atacama Large Millimeter/submillimeter Array at Band 8 with the reference frequency of 405 GHz. A submillimeter source is discovered at the radio peak of the hot spot. Because the 405 GHz flux density of the source, 80.7 ± 3.1 mJy, agrees with the extrapolation of the synchrotron radio spectrum, the far-infrared excess is suggested to exhibit no major contribution at the ACA band. In contrast, by subtracting the power-law spectrum tightly constrained by the radio and ACA data, the significance of the excess in the Herschel band is well confirmed. No diffuse submillimeter emission is detected within the ACA field of view, and thus, the excess is ascribed to the west hot spot itself. In comparison to the previous estimate based on the Herschel data, the relative contribution of the far-infrared excess is reduced by a factor of ~ 1.5 . The spectrum of the excess below the far-infrared band is determined to be harder than that of the diffusive shock acceleration. This strengthens the previous interpretation that the excess originates via the magnetic turbulence in the substructures within the hot spot. The ACA data are utilized to evaluate the magnetic field strength of the excess and of diffuse radio structure associated to the hot spot.

Keywords: Radio hot spots (1344) — Relativistic jets (1390) — Non-thermal radiation sources (1119) — Fanaroff-Riley radio galaxies(526) — Magnetic fields (994) — Radio interferometers (1345)

1. INTRODUCTION

Fanaroff–Riley type-II (Fanaroff & Riley 1974) radio galaxies generally host compact radio sources, called hot spots, at the terminal of their nuclear jets. In the standard picture, the hot spots are regarded as an ongoing site of the diffusive shock acceleration (Begelman et al. 1984), where particles are energized up to relativistic regime. As a result, they are usually recognized as a

strong synchrotron radio and inverse Compton X-ray emitter (Hardcastle et al. 2004).

Theoretical and numerical studies (e.g., Inoue et al. 2009) indicate that magnetic turbulence is induced in the post-shock region. The turbulence (e.g., Asano et al. 2014) and associated magnetic reconnection (e.g., Sironi & Spitkovsky 2014) are theoretically proposed to behave as an efficient accelerator. However, concrete signatures of these acceleration processes in the hot spots have not yet been confirmed, except for an observational suggestion by Orienti et al. (2017).

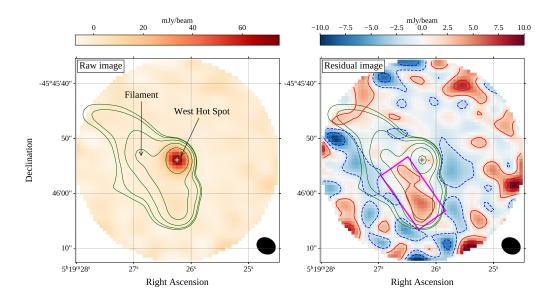


Figure 1. (left) Primary-beam-corrected ALMA ACA image at 405 GHz around the west hot spot of Pictor A, on which the ATCA 4.86 GHz image (Isobe et al. 2017, 2020) is overlaid with thin solid contours. The arrows indicate the west hot spot and filament (Röser & Meisenheimer 1987). The ALMA ACA beam is shown with the ellipse on the bottom right. The cross points the ALMA ACA position of the detected submillimeter source. (right) Residual image after subtracting the submillimeter source. The negative and positive RMS noise levels $(\pm 1\sigma$ and $\pm 3\sigma$) are displayed with the dashed and solid contours, respectively. The thick solid rectangle indicates the aperture adopted for evaluating the flux upper limit of the filament.

These acceleration processes are predicted to generate a hard particle spectrum (e.g., Asano et al. 2014; Sironi & Spitkovsky 2014) with the corresponding synchrotron spectral index of $\alpha < 0.5$ where the flux density at the frequency ν is described as $F_{\nu} \propto \nu^{-\alpha}$. This spectral slope is significantly flatter than that of the standard diffusive shock acceleration (i.e., $\alpha \geq 0.5$). As a result, the turbulence and/or re-connection accelerations are possible to dominate the synchrotron spectrum in the higher frequency range, namely in the submillimeter and/or infrared band, even if their contribution is expected to be negligible in the radio band in comparison to the standard diffusive shock acceleration.

Recent progress in infrared investigation into hot spots of nearby radio galaxies (Isobe et al. 2017, 2020; Sunada et al. 2022) hinted a possible observational evidence of the turbulence and/or magnetic re-connection acceleration. By making most of the mid-infrared (MIR) data with the Wide-field Infrared Survey Explorer (WISE) and the far-infrared (FIR) ones with the Spectral and Photometric Imaging REceiver (SPIRE; Griffin et al. 2010) onboard the Herschel observatory, Isobe et al. (2017, 2020) have discovered from the west hot spot of the radio galaxy Pictor A an excess emission in the FIR and MIR bands over the main synchrotron

component dominating the radio and optical data. They successfully indicated that the excess exhibits a very hard spectrum with an index of $\alpha=0.22\pm0.06$ below the FIR frequency range (Isobe et al. 2020). This excess was interpreted by invoking the turbulence and/or re-connection acceleration operated in 10-pc scale substructures which are resolved with the Very Long Baseline Array (VLBA) within the object (Tingay et al. 2008). However, the large SPIRE beam (17.6" for the PSW array at the wavelength of 250 μ m; Griffin et al. 2013) made it difficult to resolve the west hot spot from neighboring diffuse structures including the so-called filament (Röser & Meisenheimer 1987), and thus, prevented a definite identification of the excess with the hot spot.

In order to tackle this difficulty, an FIR or submillimeter instrument equipped with an imaging capability in a spatial scale up to $\gtrsim 15$ " with no flux loss is desirable. The Atacama Compact Array (ACA; Iguchi et al. 2009) of the Atacama Large Millimeter/submillimeter Array (ALMA) is regarded as one of the ideal instruments. Especially, when it is operated at Band 8, the ALMA ACA simultaneously achieves a reasonable beam size (~ 3 ") and a large Maximum Recoverable Size (MRS; ~ 15 "). Therefore, an ALMA ACA Band-8 observation was con-

ducted of the west hot spot of the radio galaxy Pictor A.

For the consistency to the previous studies (Tingay et al. 2008; Isobe et al. 2017, 2020), the following cosmological parameters are taken from Spergel et al. (2003); $H_0 = 71 \text{ km s}^{-1} \text{ Mpc}^{-1}$, $\Omega_{\rm m} = 0.27$, and $\Omega_{\Lambda} = 0.73$. These give an angle-to-size conversion factor of 688 pc arcsec⁻¹ at the redshift of Pictor A (z = 0.035; Eracleous & Halpern 2004).

2. OBSERVATION

The west hot spot of the radio galaxy Pictor A was targeted by the ALMA ACA at Band 8 on 2022 July 26, as a project approved for the ACA supplemental call of the ALMA Cycle 8 2021 (the project code of 2021.2.00039.S). The nominal receiver and correlator configurations for continuum observations were adopted with the representative frequency of 405 GHz. The peak position of the object, which is measured from the 4.86 GHz radio image with the Australia Telescope Compact Array (ATCA) as the right ascension and declination of $\alpha = 05^{\rm h}19^{\rm m}26.2419^{\rm s}$ and $\delta = -45^{\rm d}45^{\rm m}53.971^{\rm s}$ respectively (Isobe et al. 2017), was placed at the ACA fieldof-view center. For the bandpass, phase and flux calibrations, the following three neighbouring radio sources were observed; J0440 - 4333, J0515 - 4556 and J0538 -4405.

3. ANALYSIS AND RESULTS

The standard pipeline products with the pipeline version of 2021.2.0.128 and the Common Astronomical Software Application (CASA; McMullin et al. 2007) version of 6.2.1.7 were taken from the ALMA science archive. No manual reprocessing was performed to the pipeline products. The ALMA data were analyzed with the CASA version 6.5.1 in combination with the python astronomical packages, Astropy (Astropy Collaboration et al. 2013, 2018, 2022) and photutils.

The 405 GHz ALMA ACA interferometric image of the west hot spot of Pictor A is displayed in the left panel of Figure 1. On the ALMA image, the 4.86 GHz ATCA contour image is superposed. The figure clearly reveals a bright submillimeter source spatially associated with the west hot spot. A two-dimensional Gaussian image fitting procedure with the CASA tool imfit was applied to the detected submillimeter source with the sky level fixed at 0 mJy beam⁻¹. The resultant parameters of the submillimeter source are summarized in Table 1.

The peak position measured with the ALMA ACA (the cross in Figure 1) is found to agree with the ATCA

Table 1. Summary of the source parameters.

Category	Parameter	Value
Photometry	$F_{\nu}(405 \text{ GHz}) \text{ (mJy)}^{a}$	80.7 ± 3.1
Astrometry	α (Right Ascension)	$05^{\rm h}19^{\rm m}26.2458^{\rm s}$
	δ (Declination)	$-45^{\rm d}45^{\rm m}53.908^{\rm s}$
	$(\Delta heta_lpha,\Delta heta_\delta)^{-b}$	(0.035", 0.034")
Source shape c	$d_{ m maj}$ d	$3.73" \pm 0.09"$
	d_{\min} e	$3.21" \pm 0.07"$
	$\phi_{\mathrm{PA}} f$	$46.8^{\circ} \pm 5.7^{\circ}$
Beam shape	$d_{ m maj,b}$ d	3.55"
	$d_{ m min,b}$ e	2.92"
	$\phi_{ m PA,b} f$	61.5°

^aFlux density at the frequency of 405 GHz.

and WISE positions (Isobe et al. 2017), within ~ 75 mas and ~ 310 mas, respectively. With the typical ALMA astrometric accuracy ($\sim 5\%$ of the synthesized beam, corresponding to ~ 150 mas in this ACA image) taken into account, these positional coincidences naturally indicate a physical connection between the ATCA, ALMA and WISE sources. The beam-inclusive major and minor sizes of the source, $d_{\rm maj} = 3.73" \pm 0.09"$ and $d_{\rm min} = 3.21" \pm 0.07"$ respectively in the full width at half maximum (FWHM), are slightly larger than the synthesized ALMA ACA beam size. This suggests the intrinsic FWHM source size of $\sim 1"$ after the beam deconvolution. The integrated 405 GHz flux density of the source was measured as $F_{\nu} = 80.7 \pm 3.1$ mJy.

The right panel of Figure 1 shows the residual image derived with the imfit tool after the Gaussian profile of the detected source was subtracted. Within the annulus with a radius of r=6"–15" centered on the detected source, where the impact from the source was negligible, the root-mean-squared (RMS) noise level was estimated as $\sigma=2.02$ mJy beam⁻¹. In the residual image, the $\pm 1\sigma$ and $\pm 3\sigma$ noise levels are drawn with the solid (positive) and dashed (negative) lines. Except for the region near the edge of the field of view (e.g., $r \gtrsim 15$ ") where spatial fluctuations are enhanced by the primary-beam

^b The positional error along the right ascension and declination without any systematic errors included.

^cBefore beam deconvolution.

dThe major size in the FWHM.

^eThe minor size in the FWHM.

f_{The position angle.}

correction, no region was found to exhibit a significance higher/lower than $\pm 3\sigma$.

The residual image hints possible emission associated with the south part of the filament, although its significance is relatively low. Thus, the upper limit on its flux density was estimated from the aperture shown with the thick solid rectangle in the right panel of Figure 1. The aperture has a length and width of 12" and 6", corresponding to the physical size of 8.26 kpc and 4.13 kpc respectively, at the source frame. By supposing a spatial independence at a scale larger than the beam size, the RMS noise level was scaled by the square root of the beam number within the aperture. As a result, the ALMA ACA upper-limit flux density was derived as $F_{\nu,\mathrm{fil}} = 15.0$ mJy at the signal-to-noise (SN) ratio of 3.

4. REVISIT TO THE FIR EXCESS OF THE WEST HOT SPOT

4.1. Significance

The spectral energy distribution (SED) of the synchrotron emission from the west hot spot of Pictor A in the radio-to-optical range is shown in Figure 2. The ALMA data on this plot (the filled circle) takes into account the systematic error of the ALMA photometry at Band 8 (i.e., typically 10% ¹; $\Delta F_{\nu} = 8.1$ mJy in this case) by a root sum square. The figure clearly depicts that the ALMA flux is consistent with the simple extrapolation of the radio spectrum. The best-fit powerlaw (PL) model to the radio and ALMA data is plotted with the gray area encompassed by the solid lines (the 68% confidence range) in panel (a) of Figure 2. The model yields the 5 GHz flux density and energy index of $F_{\nu}(5 \text{ GHz}) = 2.18 \pm 0.03 \text{ Jy and } \alpha = 0.748 \pm 0.007,$ respectively. These parameters agree with those derived without the ALMA data (Meisenheimer et al. 1997). This result indicates that the FIR excess does not have a major contribution in the ALMA frequency range.

By simply extrapolating the PL model best fit to the radio and ALMA data, the FIR excess revealed with the Herschel SPIRE (Isobe et al. 2020) is evaluated. This method is expected to provide a conservative estimate on the significance of the FIR excess, since the observed high-frequency radio and submillimeter flux is possibly contaminated by the excess flux (see §4.2). Panel (a) of Figure 2 displays that the PL extrapolation (the gray area, $F_{\nu,PL}$ in Table 2) is insufficient to describe the SPIRE flux. The signal statistics of the FIR excess $(F_{\nu,ex})$ in the three SPIRE photometric bands (i.e., the PLW, PMW and PSW) are listed in Table 2. Even

Table 2. Summary of the FIR excess.

SPIRE bands	PLW	PMW	PSW
$\nu \ (10^{12} \ {\rm Hz})$	0.60	0.86	1.20
$F_{\nu} \text{ (mJy)}^a$	123.7 ± 10.9	70.0 ± 9.9	63.3 ± 10.7
$F_{\nu,\mathrm{PL}} \; (\mathrm{mJy})^{b}$	60.6 ± 1.9	46.4 ± 1.6	36.1 ± 1.3
$F_{\nu,\text{ex}} \text{ (mJy)}^{c}$	63.0 ± 11.1	23.6 ± 10.1	27.2 ± 10.8
SN ratio	5.70	2.34	2.52
$F_{\nu,\mathrm{fil}} \; (\mathrm{mJy})^d$	≤ 8.9	≤ 5.6	≤ 3.6

 $^{^{}a}$ The total FIR flux of the west hot spot taken from Isobe et al. (2020)

though adopting this conservative estimate, the significance of the FIR excess is fairly confirmed.

Thanks to its large MRS (16.5" in the FWHM at 405 GHz), the ALMA ACA image shown in Figure 1 covers with almost no flux loss the SPIRE beam at least for the PSW array (17.6" in the FWHM; Griffin et al. 2013). Importantly, the ALMA ACA data did not reveal a diffuse source with a spatial scale comparable to the SPIRE beam.

A possible contamination from the filament to the FIR excess is evaluated, by combining the radio and ALMA data (see §5 for the details). When the broken-PL (BPL) model which connects the radio data in the GHz range and the ALMA upper limit is simply extrapolated to the higher frequency range, the upper limit on the SPIRE flux of the filament $(F_{\nu,\text{fil}})$ is evaluated as tabulated in Table 2 (the arrowed squares in Figure 4). It is found that the contribution from the filament is less than $\lesssim 24\%$, and thus, a large fraction of the FIR excess is ascribed to the west hot spot itself.

4.2. Spectral interpretation

In order to investigate the FIR excess, Isobe et al. (2020) adopted a simple two-component model, where the main cutoff-PL (CPL) component describes the radio and optical data, and the BPL one subjected to the high-frequency cutoff is adopted to reproduce the excess. Because the BPL component was suggested to require a low-frequency spectral slope significantly flat-

¹ Taken from the ALMA Cycle 8 2021 Technical Handbook

b Simple extrapolation of the PL model reproducing the radio and ALMA data.

^c Excess flux over the PL model.

 $^{^{}d}$ Upper limit (SN = 3) on the filament flux density.

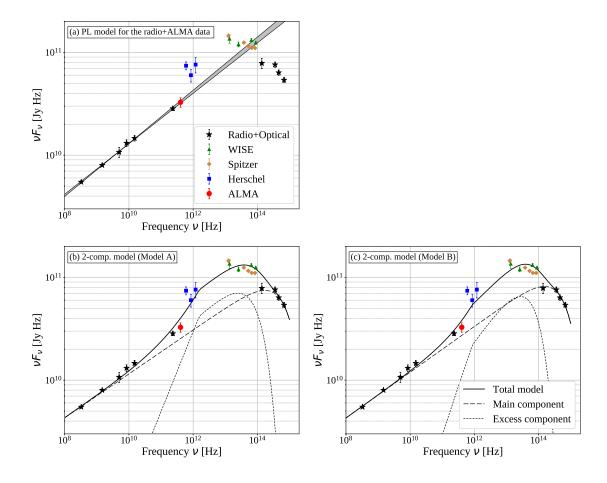


Figure 2. Synchrotron SEDs of the west hot spot of Pictor A. The ALMA data point is shown with the circle, the optical and radio data (Meisenheimer et al. 1997) are plotted with the stars, the FIR data with Herschel (Isobe et al. 2020) are displayed with the squares, and the MIR data with WISE and Spitzer (Isobe et al. 2017, and reference therein) are shown with the triangles and diamonds, respectively. In panel panel (a), the best-fit PL model to the radio and ALMA data is shown with the gray area encompassed with the two solid lines (the 68% confidence region). In panels (b) and (c), the two-component model originally proposed in Isobe et al. (2020) is plotted with the thick solid line, with the dashed and dotted lines indicating the main CPL and excess BPL components, respectively. The spectral parameters are taken from Isobe et al. (2020) (Model A in Table 3) in panel (b), while all the the parameters are tuned by including the ALMA data (Model B) in panel (c).

ter than that of the diffusive shock acceleration, they invoked for the FIR excess the turbulence acceleration (e.g., Asano et al. 2014) and/or magnetic re-connection one (e.g., Sironi & Spitkovsky 2014). In addition, the substructures inside the object resolved with the VLBA (Tingay et al. 2008) were proposed as the acceleration site, since the sum flux of the substructures at 1.67 GHz was found to agree with the BPL flux.

Table 3 tabulates eight controlling parameters of the two-component model; the flux density at a given frequency $(F_{\nu,m})$, spectral index (α_m) , and cutoff frequency $(\nu_{c,m})$ of the main CPL component, and the flux density $(F_{\nu,e})$, spectral indices below and above the break $(\alpha_{\text{low},e})$ and $\alpha_{\text{high},e}$, the break and cutoff frequencies $(\nu_{b,e})$ and $\nu_{c,e}$ of the excess BPL component. The standard cooling break under the continuous energy injec-

tion condition ($\Delta \alpha = \alpha_{\rm high,e} - \alpha_{\rm low,e} = 0.5$; Carilli et al. 1991) is adopted for the BPL component. The result in Isobe et al. (2020) is referred to as Model A in Table 3, and the corresponding model curve is shown in panel (b) of Figure 2. The ALMA data does not necessarily reject Model A, because their deviation is estimated as a significance of only SN ~ 2.1 .

By including the ALMA data, the spectral parameters are tuned for a better solution. The best-fit model is displayed in panel (c) of Figure 2, and the corresponding SED parameters are listed in Table 3 (Model B). While most parameters are found to remain relatively unchanged from Model A, the relative contribution of the excess in the FIR-to-MIR band is reduced by a factor of ~ 1.5 , because the ALMA data, consistent with the simple radio-PL extrapolation, gives a tight constraint.

Component	Parameters	Model A^a	Model B^b
Main CPL	$F_{\nu,\mathrm{m}}(5 \mathrm{~GHz}) \mathrm{~(Jy)}$	1.98 ± 0.09	2.05 ± 0.11
	$lpha_{ m m}$	0.79 ± 0.02	0.78 ± 0.02
	$\nu_{\rm c,m}~({\rm Hz})$	$8.0^{+3.9}_{-2.6} \times 10^{14}$	$6.8^{+3.0}_{-2.1} \times 10^{14}$
Excess BPL	$F_{\nu,e}(1.67 \text{ GHz}) \text{ (mJy)}$	121.3 (fix)	38^{+281}_{-34}
	$lpha_{ m low,e}$	0.22 ± 0.06	0.06 ± 0.35
	$lpha_{ m high,e}$ c	$lpha_{ m low,e} + 0.5$	
	$ u_{ m b,e} \left({ m Hz} \right)$	$1.6^{+3.0}_{-1.0} \times 10^{12}$	$8.6^{+90.4}_{-7.8} \times 10^{11}$
	$\nu_{\rm c.e.}$ (Hz)	$8.8^{+3.4}_{2.4} \times 10^{13}$	$6.3^{+5.8}_{-2.0} \times 10^{13}$

Table 3. Summary of the SED parameters.

The 1.67 GHz flux density of the BPL component for the FIR excess, $F_{\nu,e}(1.67 \text{ GHz}) = 38^{+281}_{-34} \text{ mJy}$ in Model B, is still consistent to the sum flux density of the substructures (121.3 mJy; Tingay et al. 2008) though with a large error in $F_{\nu,e}(1.67 \text{ GHz})$. Especially, the lowfrequency spectral index of the excess BPL component, revised as $\alpha_{\text{low,e}} = 0.06 \pm 0.35$, is confirmed to be significantly harder than that of the diffusive shock acceleration ($\alpha = 0.5$ for the strong shock limit). Instead, this value agrees with the prediction from the turbulence acceleration ($\alpha = 0$; Asano et al. 2014) under the hard-sphere condition (Park & Petrosian 1995). Additionally, the intrinsic size of the ALMA source, ~ 1 ". is comparable to the distance among the substructures. These results strengthen the scenario that the FIR excess is produced through the turbulence acceleration operated in the VLBA substructures (Isobe et al. 2020).

4.3. physical condition

The magnetic field for the FIR excess of the west hot spot is evaluated after Isobe et al. (2020). When the observed break is ascribed to the radiative cooling, the break frequency is converted into the magnetic field as

$$B^3 \simeq \frac{27\pi e m_{\rm e} v^2 c}{\sigma_{\rm T}^2} L_{\rm cool}^{-2} \nu_{\rm b}^{-1},$$
 (1)

where e is the electron charge, $m_{\rm e}$ is the electron rest mass, $\sigma_{\rm T}$ is the Thomson cross section, v is the down flow speed in the shock frame, c is the speed of light, and $L_{\rm cool}$ is the cooling length during which the impact of the radiative cooling on the electrons at the break becomes effective (Inoue & Takahara 1996).

Here, the VLBA substructures inside the object are regarded as the origin of the FIR excess after Isobe et al.

(2017, 2020). The minor length of the individual substructures (28–58 pc; Tingay et al. 2008) is adopted as the cooling length, since their minor axis is nearly aligned to the jet toward the west hot spot. The flow speed is assumed as $v \sim 0.3c$ (Kino & Takahara 2004). Thus, the cooling break frequency of the FIR excess, $\nu_{\rm b,e} = 8.6^{+90.4}_{-7.8} \times 10^{11}$ Hz (Model B), is transformed to the magnetic field as B = 0.86-7.2 mG by Equation (1).

Alternatively, the magnetic field under the minimum-energy condition is widely adopted as a standard indicator for synchrotron sources (Miley 1980). The shape of the emission region is assumed to be a simple disk, of which the height and diameter, respectively, equal to the minor and major lengths of the substructures (87–170 pc for the latter; Tingay et al. 2008). The lowest synchrotron frequency of $\nu_{\rm min}=10$ MHz is adopted after Miley (1980), and the proton contribution is simply neglected. As a result, the determined spectrum of the FIR excess roughly yields the minimum-energy magnetic field as $B_{\rm me}=280$ –480 $\mu{\rm G}$. Importantly, the magnetic field from the cooling break is found to be higher than the minimum-energy value as $B/B_{\rm me}=2$ –26.

Several ideas are briefly discussed to reconcile this discrepancy. The above $B_{\rm me}$ value is possibly underestimated due to undetectable plasma contents. Firstly, the contribution from low-energy electrons is considered. The existence of the low-energy electrons with a Lorentz factor of $\gamma_{\rm e} \ll 100$ associated to the jets and hot spots is under debate (e.g., Brunetti et al. 2001). However, owing to the spectral hardness of the FIR excess, the minimum-energy magnetic field is found to stay unchanged, even if the minimum synchrotron frequency is lowered down to $\nu_{\rm min} = 2$ kHz, which corresponds to $\gamma_{\rm e} \sim 1$ for the inferred $B_{\rm me}$ value.

aCase 2 in Isobe et al. (2020)

^b All the parameters are revised with the ALMA data included.

^c The standard cooling break condition (Carilli et al. 1991) is assumed.

The second alternative is the proton contribution. The above calculation conservatively assumes the proton-to-electron energy ratio of k=0, because the proton is invisible through the synchrotron emission. If the protons have a significant energy dominance of $k\sim 1000$, the minimum-energy magnetic field is enhanced up to $B_{\rm me}=2\text{--}3.5~\rm mG$. Thus, the observed cooling break becomes consistent to the minimum-energy condition. However, such a high proton dominance is possibly doubtful in Fanaroff–Riley type-II sources (e.g., Kawakatu et al. 2016; Kino et al. 2012).

Finally, a physical mechanism to strengthen the magnetic field is invoked to interpret the inconsistency between the cooling break and minimum-energy condition. It is theoretically predicted that the post-shock turbulence is possible to amplify the magnetic field by more than a factor of 10 (e.g., Inoue et al. 2009; Mizuno et al. 2011). This mechanism is successfully applied to X-ray shells, rims and hot spots found in Galactic supernovae remnants (e.g., Bamba et al. 2003; Uchiyama et al. 2007). As is indicated in Isobe et al. (2020), the magnetic amplification by the post-shock turbulence is well matched to the value of $B/B_{\rm me}=2$ –26 obtained by including the ALMA data. This idea also seems compatible with the interpretation that the FIR excess is produced via the turbulence acceleration.

4.4. additional notes

Before closing the discussion on the properties of the FIR excess, this subsection briefly presents several concerns to be settled through future observations. In spite of their frequency proximity, the total flux density of the west hot spot measured with the SPIRE PLW at 600 GHz (see Table 2) is by a factor of ~ 1.5 higher than that with the ALMA ACA at 405 GHz (tabulated in Table 1). Accordingly, the spectrum in this narrow range appears to be steeply "rising" with a corresponding two-point spectral index of $\alpha \sim -1.0$. Contamination from point sources is probably rejected as discussed in §3, since no significant source is detected on the ALMA ACA image shown in Figure 1, of which the field of view is comparable to the SPIRE PLW beam (the FWHM size of 35.2"; Griffin et al. 2013). However, strictly speaking, this PLW beam is not fully covered with the MRS of the ALMA ACA at 405 GHz. Then, it is potential for the PLW flux density to have been affected by unidentified diffuse emission with a scale of $\gtrsim 16.5$ ". In contrast, as mentioned in §4.1, the higher-frequency SPIRE results are basically regarded as more reliable, since the SPIRE beam at these bands is comparable to the ALMA ACA MRS.

The substructures are previously resolved only in the 1.67 GHz VLBA observation (Tingay et al. 2008). Correspondingly, there is a very wide frequency gap in more than 2 orders of magnitude between the substructures and FIR excess. In addition, due to the low declination of Pictor A ($\delta \sim -46^{\circ}$), the VLBA observation was conducted in a relatively severe observational condition with only 5 southern VLBA antennas at a low elevation angle (namely $\lesssim 13^{\circ}$). For better understanding the substructures, it is important to obtain high-resolution images with a higher dynamic range in improved observational conditions. Such observations are expected to be enabled by future very long baseline interferometric observatories, especially in the southern hemisphere.

Finally, there is possible room for improvement in the spectral modeling. Panel (c) of Figure 2 suggests that the BPL model (Model B in Table 3) appears to underestimate slightly the FIR flux density, although the deviation between the modeled and measured flux densities is insignificant. A current lack in spatially resolved spectral data (e.g., sufficiently better than ~ 1 ") especially over the submillimeter, FIR and MIR ranges is thought to have made it difficult to determine precisely the spectral shape of the FIR excess.

By making most of ALMA, most of the above issues are probably cleared up. ALMA observations with an angular resolution of $\lesssim 100$ mas enables to identify the submillimeter counterpart to the VLBA substructures. The Square Kilometer Array is similarly thought to be useful to derive a radio insight into the substructures. In addition, a combination of the Near Infrared Camera and Mid-Infrared Instrument onboard the James Webb Space Telescope is expected to give a great progress in understanding the FIR excess.

5. PROPERTIES OF THE FILAMENT

The ALMA ACA data is also useful to infer the physical condition in the filament. The relativistic plasma filling the filament is thought to be supplied from the west hot spot through back or lateral flows (Mizuta et al. 2010; Saxton et al. 2002). Thus, immediately after the plasma is injected into the filament, its synchrotron spectral index in the GHz range is simply supposed to be same as that of the main component in the spectrum of the west hot spot ($\alpha_{\rm m} = 0.78 \pm 0.02$ for Model B). The radio data obtained with the Very Large Array (VLA) basically support this idea, since the spectral index of the filament in the 5–15 GHz range measured with VLA $(\alpha \sim 0.8; \text{ Perley et al. 1997})$ is consistent to the index of the main component. In contrast, electrons in the filament radiating the synchrotron emission at the ALMA band are expected to be already subjected to the ra-

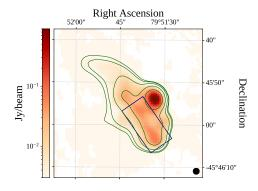


Figure 3. The 8.44 GHz VLA image of the west hot spot of Pictor A (Perley et al. 1997), displayed after the astrometric correction. The 4.86 GHz ATCA image, shown in Figure 1, is superposed with the thin contours. The photometric aperture for the filament is plotted with the thick solid rectangle. The filled circle on the bottom right indicates the VLA beam with the FWHM size of 1.5".

diative cooling, since the ALMA flux of the filament is insignificant, as shown in §3. These indicate that the filament exhibits the cooling break between the VLA and ALMA frequency ranges.

A combination of the VLA and ALMA data are utilised to quantitatively evaluate the cooling break frequency of the filament. Here, the VLA images at the frequency of 4.87, 8.44, and 14.96 GHz with a beam size of 1.5" are adopted from Perley et al. (1997). The lowerfrequency VLA data presented in Perley et al. (1997), i.e. in the range of 74 MHz – 1.4 GHz, are not employed in the following investigation, since their beam size is found to be insufficient to resolve the filament from the west hot spot. It is noticed that the adopted VLA images are affected by an astrometric error in an angular scale of $\lesssim 0.7$ ". Thus, the sky coordinates of the VLA images are corrected by referring to the peak position of the west hot spot on the 4.86 ATCA image in Figure 1, because the astrometry of this ATCA image was previously validated within ~ 20 mas in Isobe et al. (2017). Figure 3 presents the 8.44 GHz VLA image around the west hot spot after the astrometric correction, in comparison to the ATCA image. The ATCA image is omitted in the following photometric analysis due to its larger beam size (~ 2.5 "), although it was checked that the 4.86 GHz ATCA flux density of the filament agrees with the 4.87 GHz VLA one within $\sim 3\%$.

The VLA flux density of the filament is integrated within the same photometric aperture as for the ALMA image, which is replotted in Figure 3 with the thick solid rectangle. The 8.44 GHz flux density of the filament is measured as $F_{\nu,\mathrm{fil}} = 0.80 \pm 0.04$ Jy with VLA. Here, the typical systematic error of the VLA photo-

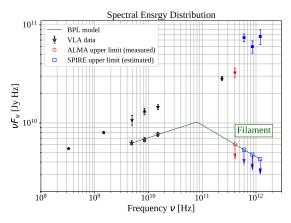


Figure 4. The synchrotron SED of the filament. The open stars show the VLA data, while the arrowed open circle indicates the ALMA upper limit. The BPL model connecting the VLA and ALMA data is drawn with the solid line, where the spectral index below the break is determined from the PL fitting to the VLA data ($\alpha_{\rm fil}=0.82\pm0.06$) and the standard cooling break condition is assumed ($\Delta\alpha=0.5$). The upper limit on the SPIRE flux, evaluated from the simple BPL extrapolation, is plotted with the arrowed open squares. For comparison, the spectrum of the west hot spot is displayed by adopting the same symbol notation as for Figure 2.

metric calibration (5%; Perley & Butler 2017) is conservatively adopted. The SED of the filament is displayed in Figure 4. The obtained VLA spectrum, shown with the open stars in Figure 4, is well reproduced by a single PL model. The spectral index, derived as $\alpha_{\rm fil} = 0.82 \pm 0.06$, is confirmed to agree with the result reported in Perley et al. (1997).

The ALMA upper limit on the flux density of the filament, which is plotted with the open circle accompanied with the downward arrow in Figure 4, is found to be significantly below the simple extrapolation of the PL model to the VLA data. Thus, it is demonstrated that the cooling break of the filament is located between the VLA and ALMA bands. The PL model to the VLA data is connected to the ALMA upper limit by introducing a simple break (i.e., the BPL model), as drawn with the solid line in Figure 4. Here, the standard cooling break condition of $\Delta \alpha = 0.5$ is employed. As a result, the cooling break frequency of the filament is evaluated as $\nu_{\rm b,fil} \lesssim 8 \times 10^{10}$ Hz.

By utilizing equation (1), the magnetic field of the filament is calculated from the break frequency. For the evaluation, two representative cases are considered for the cooling length; the distance between the hot spot and filament along the jet $(L_{\text{cool},1} \sim 3.4 \text{ kpc})$ or 5") and the width of the filament perpendicular to the jet toward the filament aperture for the flux evaluation $(L_{\text{cool},2} \sim 6.2 \text{ kpc})$ or 9"). In either case, the back (for

 $L_{\rm cool,1}$) or lateral (for $L_{\rm cool,2}$) flow speed of $v\sim 0.3c$ (Perley et al. 1997; Kino & Takahara 2004) is adopted. The magnetic field strength in the filament is evaluated from the derived value of $\nu_{\rm b,fil}$ as $B_1\gtrsim 280~\mu{\rm G}$ and $B_2\gtrsim 190~\mu{\rm G}$ for $L_{\rm cool,1}$ and $L_{\rm cool,2}$, respectively. The magnetic field of the filament is suggested to be by a factor of ~ 3 –40 weaker than that of the FIR excess from the west hot spot.

By utilizing the BPL spectrum connecting the VLA and ALMA data and adopting the rectangular aperture in Figures 1 (b) and 3, a crude estimated on the minimum-energy magnetic field of the filament is given as $B_{\rm me} \sim 30~\mu{\rm G}$. Similar to the FIR excess, the filament is found to exhibit a high value of $B/B_{\rm me} \sim 5$ –10. These indicate that the turbulence also plays an important role in the filament.

The authors are grateful to the anonymous reviewer for suggestive comments. The ALMA data with the following code are utilized in the present study; ADS/JAO.ALMA#2021.2.00039.S. ALMA is a partnership of ESO (representing its member states), NSF (USA) and NINS (Japan), together with NRC (Canada), MOST and ASIAA (Taiwan), and KASI (Republic of Korea), in cooperation with the Republic of Chile. The Joint ALMA Observatory is operated by ESO, AUI/NRAO and NAOJ. The VLA images of the west hot spot of Pictor A in the electric form are kindly provided by Dr. R. A. Perley. The ATCA data of Pictor A were originally provided by Dr. E. Lenc at the time of Isobe et al. (2017). This research is supported by the JSPS KAKENHI grants No. JP18K03709, JP21H01137, JP21H04496, JP21K03635, and JP22H00157. This research is aided by the ALMA Japan Research Grant of NAOJ ALMA Project, NAOJ-ALMA-276.

Software: CASA (McMullin et al. 2007), Astropy (Astropy Collaboration et al. 2013, 2018, 2022), photutils

REFERENCES

Asano, K., Takahara, F., Kusunose, M., Toma, K., & Kakuwa, J. 2014, ApJ, 780, 64, doi: 10.1088/0004-637X/780/1/64

Astropy Collaboration, Robitaille, T. P., Tollerud, E. J., et al. 2013, A&A, 558, A33,

 $\mathbf{doi:}\ 10.1051/0004\text{-}6361/201322068$

Astropy Collaboration, Price-Whelan, A. M., Sipőcz, B. M., et al. 2018, AJ, 156, 123, doi: 10.3847/1538-3881/aabc4f

Astropy Collaboration, Price-Whelan, A. M., Lim, P. L., et al. 2022, ApJ, 935, 167, doi: 10.3847/1538-4357/ac7c74

Bamba, A., Yamazaki, R., Ueno, M., & Koyama, K. 2003, ApJ, 589, 827, doi: 10.1086/374687

Begelman, M. C., Blandford, R. D., & Rees, M. J. 1984, Reviews of Modern Physics, 56, 255, doi: 10.1103/RevModPhys.56.255

Brunetti, G., Cappi, M., Setti, G., Feretti, L., & Harris,
D. E. 2001, A&A, 372, 755,
doi: 10.1051/0004-6361:20010484

Carilli, C. L., Perley, R. A., Dreher, J. W., & Leahy, J. P. 1991, ApJ, 383, 554, doi: 10.1086/170813

Eracleous, M., & Halpern, J. P. 2004, ApJS, 150, 181, doi: 10.1086/379823

Fanaroff, B. L., & Riley, J. M. 1974, MNRAS, 167, 31P, doi: 10.1093/mnras/167.1.31P Griffin, M. J., Abergel, A., Abreu, A., et al. 2010, A&A, 518, L3, doi: 10.1051/0004-6361/201014519

Griffin, M. J., North, C. E., Schulz, B., et al. 2013, MNRAS, 434, 992, doi: 10.1093/mnras/stt999

Hardcastle, M. J., Harris, D. E., Worrall, D. M., & Birkinshaw, M. 2004, ApJ, 612, 729, doi: 10.1086/422808

Iguchi, S., Morita, K.-I., Sugimoto, M., et al. 2009, PASJ, 61, 1, doi: 10.1093/pasj/61.1.1

Inoue, S., & Takahara, F. 1996, ApJ, 463, 555, doi: 10.1086/177270

Inoue, T., Yamazaki, R., & Inutsuka, S.-i. 2009, ApJ, 695, 825, doi: 10.1088/0004-637X/695/2/825

Isobe, N., Koyama, S., Kino, M., et al. 2017, ApJ, 850, 193, doi: 10.3847/1538-4357/aa94c9

Isobe, N., Sunada, Y., Kino, M., et al. 2020, ApJ, 899, 17, doi: 10.3847/1538-4357/ab9d1c

Kawakatu, N., Kino, M., & Takahara, F. 2016, MNRAS, 457, 1124, doi: 10.1093/mnras/stw010

Kino, M., Kawakatu, N., & Takahara, F. 2012, ApJ, 751, 101, doi: 10.1088/0004-637X/751/2/101

Kino, M., & Takahara, F. 2004, MNRAS, 349, 336, doi: 10.1111/j.1365-2966.2004.07511.x

McMullin, J. P., Waters, B., Schiebel, D., Young, W., & Golap, K. 2007, in Astronomical Society of the Pacific Conference Series, Vol. 376, Astronomical Data Analysis Software and Systems XVI, ed. R. A. Shaw, F. Hill, & D. J. Bell, 127

- Meisenheimer, K., Yates, M. G., & Roeser, H. J. 1997, A&A, 325, 57
- Miley, G. 1980, ARA&A, 18, 165, doi: 10.1146/annurev.aa.18.090180.001121
- Mizuno, Y., Pohl, M., Niemiec, J., et al. 2011, ApJ, 726, 62, doi: 10.1088/0004-637X/726/2/62
- Mizuta, A., Kino, M., & Nagakura, H. 2010, ApJL, 709, L83, doi: 10.1088/2041-8205/709/1/L83
- Orienti, M., Brunetti, G., Nagai, H., et al. 2017, MNRAS, 469, L123, doi: 10.1093/mnrasl/slx067
- Park, B. T., & Petrosian, V. 1995, ApJ, 446, 699, doi: 10.1086/175828
- Perley, R. A., & Butler, B. J. 2017, ApJS, 230, 7, doi: 10.3847/1538-4365/aa6df9

- Perley, R. A., Roser, H.-J., & Meisenheimer, K. 1997, A&A, 328, 12
- Röser, H.-J., & Meisenheimer, K. 1987, ApJ, 314, 70, doi: 10.1086/165039
- Saxton, C. J., Sutherland, R. S., Bicknell, G. V., Blanchet,
 G. F., & Wagner, S. J. 2002, A&A, 393, 765,
 doi: 10.1051/0004-6361:20021004
- Sironi, L., & Spitkovsky, A. 2014, ApJL, 783, L21, doi: 10.1088/2041-8205/783/1/L21
- Spergel, D. N., Verde, L., Peiris, H. V., et al. 2003, ApJS, 148, 175, doi: 10.1086/377226
- Sunada, Y., Isobe, N., Tashiro, M. S., et al. 2022, MNRAS, 512, 5995, doi: 10.1093/mnras/stac826
- Tingay, S. J., Lenc, E., Brunetti, G., & Bondi, M. 2008, AJ, 136, 2473, doi: 10.1088/0004-6256/136/6/2473
- Uchiyama, Y., Aharonian, F. A., Tanaka, T., Takahashi,T., & Maeda, Y. 2007, Nature, 449, 576,doi: 10.1038/nature06210